

AWEsome: An open-source test platform for airborne wind energy systems

Philip Bechtle^a, Thomas Gehrman^b, Christoph Sieg^c, Udo Zillmann^d *

1st May 2017

Abstract

In this paper we present AWEsome (Airborne Wind Energy Standardized Open-source Model Environment), a test platform for airborne wind energy systems that consists of low-cost hardware and is entirely based on open-source software. It can hence be used without the need of large financial investments, in particular by research groups and startups to acquire first experiences in their flight operations, to test novel control strategies or technical designs, or for usage in public relations. Our system consists of a modified off-the-shelf model aircraft that is controlled by the `pixhawk` autopilot hardware and the `ardupilot` software for fixed wing aircraft. The aircraft is attached to the ground by a tether. We have implemented new flight modes for the autonomous tethered flight of the aircraft along periodic patterns. We present the principal functionality of our algorithms. We report on first successful tests of these modes in real flights.

* Author names are in alphabetical order.

^a Universität Bonn, bechtle@physik.uni-bonn.de

^b Universität Bonn, thomasgehrmann@gmx.net

^c Humboldt-Universität zu Berlin, csieg@physik.hu-berlin.de

^d Daidalos Capital, zillmann@daidalos-capital.com

awesome.physik.uni-bonn.de

1 Introduction

Airborne wind energy (AWE) systems are devices that convert wind energy into mechanical and ultimately electrical power via an aerodynamically active part that is at most flexibly connected to a ground station via one or several tethers. The lift force acting on the airborne part for compensating the gravitational force can either be a static buoyant force generated by lighter-than-air structures such as balloons or it can be dynamically generated in cross-wind flight.

The concept of extracting wind energy via an airborne system in cross-wind flight has been investigated more than 35 years ago by Loyd in his seminal paper [1]. Loyd determined the amount of mechanical power an aircraft that is attached to the ground via a tether can in principle harvest from a wind field. The maximal mechanical power output is given by

$$P_{\max} \lesssim \frac{2}{27} \rho A v_w^3 C_L \left(\frac{C_L}{C_D} \right)^2 \cos^3 \gamma. \quad (1)$$

Here, A , C_L and C_D are the wing area, lift and drag coefficients of the aircraft, respectively. Moreover, v_w is the wind velocity and ρ is the air density. In addition, the effect of a non-vanishing inclination angle γ that is the angle between the wind velocity vector and the vector that points along a straight tether from the attachment point on the ground to the aircraft has been considered. In case of a horizontal wind field, this angle is identical to the elevation angle of the ideal (straight) tether connecting the ground station and aircraft. The maximal power (1) is reached for a particular value for the apparent air speed v_a felt by the aircraft. This can be achieved by adjusting the drag coefficients of the on-board generators in case of drag-mode operation and the reel-out speed of the tether in case of a pumping mode operation, respectively.

For aircraft with rigid wings which have $C_L \simeq 1$ and $\frac{C_L}{C_D} \gg 1$ the possible power output is surprisingly high [2]. These and further advantages such as the possibility to harvest steadier and stronger winds at higher altitudes and the reduction of material costs compared to conventional wind turbines make AWE a very promising candidate for contributing significantly to solving the world's sustainable energy problem [2]. Vivid research and development of AWE systems is already performed by academic research groups and startup companies; see e.g. [2] for an overview of activities. A comprehensive review of the different design approaches is also given in [3, 4]. A short introduction into the economic viability is given in [5].

Especially the need to design and build the required hardware and to potentially damage or even lose it in field tests impose high economic risks on small research groups and companies. Besides that, there exist various different strategies and guidelines especially for the aircraft design and power conversion, and it is not yet clear which of them maximizes the efficiency of the system.

The purpose of our research is to provide an open-source (OS) cost-efficient and hence, in case of a failure, disposable test platform for AWE systems. We call it AWESome, the Airborne Wind Energy Standardized Open-source Model Environment.

This platform enables especially teams with small financial resources to start gaining experience in autonomous flight operations, test their deployment strategy, realize various designs in hardware or software, and to test them even allowing the risk of total loss.¹

In addition to the abovementioned consideration, the OS approach offers considerable potential advantages for the AWE industry as a whole. The development of safe, certified and efficient control algorithms is amongst the key prerequisites to finally commercialize AWE systems. The scrutiny offered by the OS approach should be seen as an important asset for maximizing safety, reliability and efficiency. We also believe that as long as the most efficient design has not been identified, close collaboration and exchange of results will accelerate the technological development and hence be advantageous for all companies for developing their individual commercial systems.

One of the key aspects of this paper is the description of the OS autopilot which allows autonomous flight of the AWESome system, and of the theoretical foundations and embedding of the control algorithms which are used to navigate along the desired periodic flight path. Besides the basic control strategy which is suitable for the limited computing capacity of the `pixhawk` microcontroller and which is described in this paper, a lot of research has been invested into the control of different types of cross-wind AWE systems. This research can be classified in several ways, for instance according to the location of the control system and actuators. Some approaches have ground-based controllers and actuators that control the airborne part via multiple tethers (see e.g. [7]) or in addition an airborne actuator (see e.g. [8]). They require models for the tethers. Others have a separate airborne control unit from which a bridle originates for the control of a soft wing (see e.g. [9]). Furthermore, the control unit and actuators can be part of a (rigid) aircraft to which only a single tether is attached (see e.g. [10]). Also, we can classify different approaches according to their employed control strategies. For instance, optimal control has been applied for maximizing the average power output [11], in addition also considering the electrical power conversion [12]. Approaches based on nonlinear model predictive control are presented in [13, 14]. For recent developments concerning further more advanced control strategies of AWE systems, see also [15, 16, 17, 18, 19, 20, 21, 22, 23]. However, in this paper we will stick to a simple proportional-differential (PD) controller for lateral navigation. Our aim is to demonstrate that even an elementary setup is sufficient for tethered flight and hence is a suitable intuitively understandable starting point for developing and testing various aspects of AWE systems.

In this paper, we will present our design platform, introduce our concepts on which our implementations of flight modes at a tether of constant length rely and discuss first results from field tests. Finally, we will give an outlook for the further development of the platform. Some complementary details can also be found in the master thesis of one of us [24].

¹Similar in spirit, another test platform based on a model plane is presented in [6] for testing autonomous take-off.

2 Foundations of the test platform

In the following, we describe the hard- and software of the test platform and its modifications. Moreover, we summarize the foundations on which our algorithms for tethered flight modes are based. Some complementary details especially concerning the hardware modifications and the implementation of the algorithms can be found in the master thesis of one of us [24]. Throughout the text we use the `typewriter` font to indicate proper names of hard- and software and of functions and variables of the source code.

2.1 Hard- and Software

The airborne part of the test platform is an off-the-shelf polystyrene model aircraft, the Easy Star II², which we modified for tethered flight. Its control surfaces are the flaps, ailerons and rudder, and it has an electric throttle. We reinforced the aircraft with carbon fabric of specific weight 160g/m² that is laminated onto the wings and bottom of the fuselage with epoxy resin. Thereby, the separate left and right wing have been glued together to a single indecomposable structure. This ensures that the aircraft can sustain the tethered flight in which the tether force acts like a payload excess. The tether is tied to a carbon tube that sits inside the wings and replaces the fiberglass tube originally delivered with the model. Moreover, the tube rests on carbon ribs that we have placed into the wings in order to transfer the force to the carbon fabric. At the expense of only adding about 150 grams of extra mass, the carbon structures significantly increase the stiffness of the aircraft. Moreover, the forces that the reinforced aircraft can sustain can be at least an order of magnitude higher than those admissible for the aircraft without modifications. We checked this with several material samples. More details of the modifications can be found in the master thesis of one of us [24]. A picture of the components is presented in figure 1.

The ground station is currently a simple fishing rod with an offshore fishing reel mounted, which serves for manually reeling in and out the tether. In comparison to a standard fishing reel, the offshore fishing reel has the advantage that its reeling technique does not twist the tether.

The autopilot that controls the aircraft consists of the `pixhawk` circuit board [25] and the `ardupilot` software [26], release 3.6.0 of June 6, 2016. The `pixhawk` contains accelerometers, gyroscopes, magnetometers and a barometer. A GPS receiver and an airspeed sensor are externally connected and communicate with the `pixhawk` via the I²C bus [27]. For manual flight, an RC receiver is also connected to the `pixhawk`. Moreover, a WLAN transmitter employs the micro air vehicle communication protocol MAVLink [28] to send and receive telemetry data to and respectively from a ground control station (GCS).

The `ardupilot` software is written in C++, and it encompasses vehicle specific codes for copters, rovers and fixed-wing aircraft. The code for fixed-wing aircraft that is

²See e.g. <https://www.multiplex-rc.de/produkte/264260-rr-easystar-ii-mit-bl-antrieb>

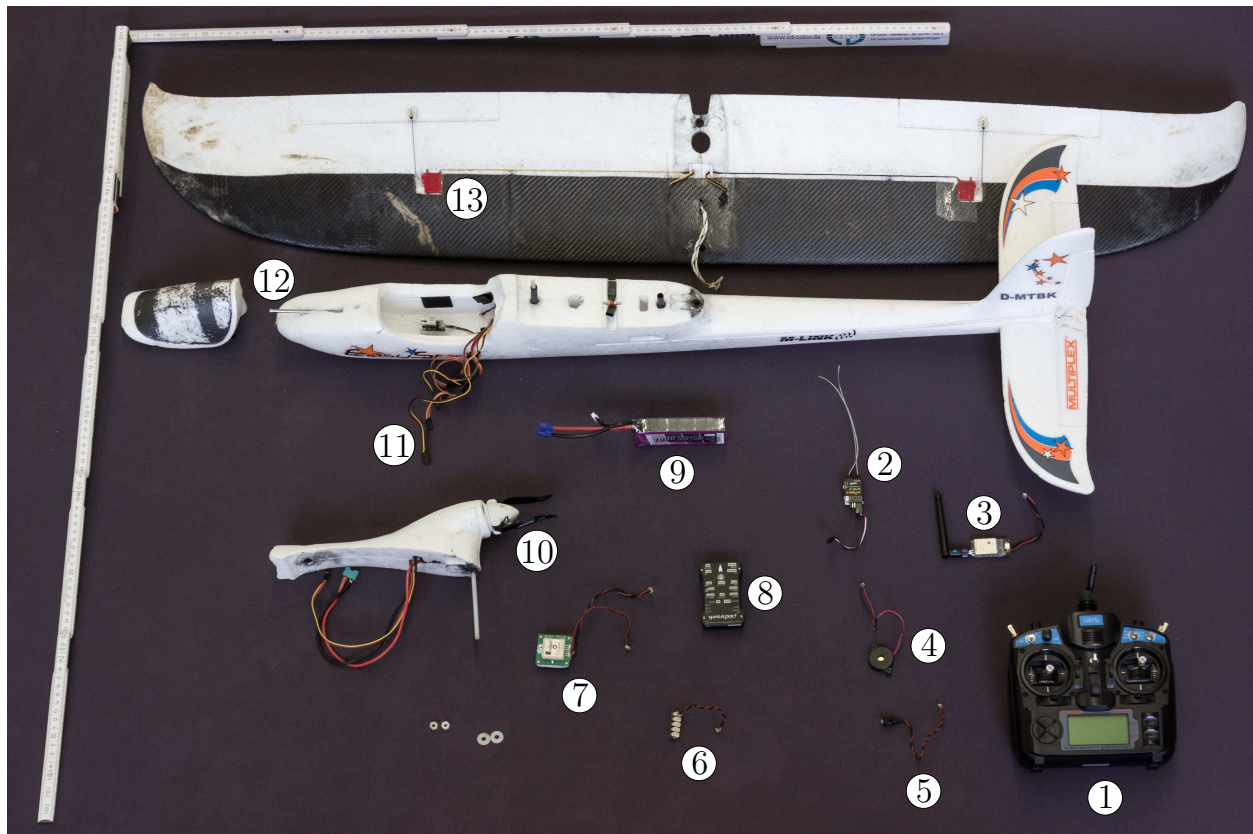


Figure 1: *Components of the modified aircraft.*

1 transmitter for remote radio control, **2 receiver** to receive signals from the transmitter, **3 telemetry** used for communication between the GCS and aircraft, **4 buzzer** makes sounds to inform about status, **5 safety switch** to prevent from accidental arming, **6 I²C splitter** provides three additional ports for digital peripherals, **7 GPS/compass module** provides positioning and heading data, **8 pixhawk** microcontroller including acceleration sensors, gyroscopes, magnetometers, barometers **9 battery** provides power, **10 propeller** provides thrust, **11 connection cables** to servos, **12 airspeed sensor** measures apparent airspeed, **13 servos** to steer the ailerons; servos for rudder and elevator are inside the fuselage

the relevant one here is denoted as ArduPlane. Each vehicle-specific code can be compiled for different target hardware, including the pixhawk, and also for a software in the loop (SITL) target. The latter allows to test the software e.g. in the OS flight dynamics model JSBSim [29].

Finally, the GCS is a laptop with Mission Planner [30] or APM Planner [31] running on its Windows or Linux operating system, respectively. For SITL simulations, JSBSim uses MAVProxy [32] as GCS.

2.2 Foundations of the tethered flight patterns

Suppose the aircraft is attached via a tether to a fixed point on the ground, denoted as ‘home’ location in the following. The tether of cross section A_t shall have a fixed

length l_0 if no force is applied, and its length l and stress τ shall increase linearly with the applied tether force F_t . The tether force and stress as a function of the length then read

$$F_t = K_t(l - l_0)\theta(l - l_0) , \quad \tau = \frac{F_t}{A_t} , \quad (2)$$

where K_t is a constant depending on the material and θ is the Heavyside step function.

An aircraft that flies attached to such a tether and keeps $\tau > 0$ constant is confined to a hemisphere of radius $R = l(\tau) = l_0 + \frac{A_t}{K_t}\tau$ that is centered around the ‘home’ location. Hence, all flight paths that are subject to this condition are curves on that hemisphere. What is important for the later analysis is that the simple model (2) incorporates the fact that at constant tether length the distance of the aircraft’s position should be a measure for the tether stress and hence the possible power output. This allows us to make some qualitative statements about the tether force even in the present case where a direct measurement of that force is not yet implemented. Of course, the simple relation (2) that is based on Hook’s law for ideal springs, is only an idealization. A more realistic model should also consider that the drag force that acts when the tether is moved through the air and the gravitational force let the tether run along a curve rather than a straight line, thereby decreasing the distance of the aircraft to the ‘home’ location at constant tether length and stress. Moreover, accelerations of the aircraft may excite oscillations of the tether. Here, we will refrain from including these effects.

The simplest periodic curve on a hemisphere is a circle. However, flying along a circle leads to a cumulation of twist on the tether. In order to avoid this, the aircraft can e.g. fly along a curve consisting of two (circular) segments of opposite orientation, resembling e.g. the figure eight. Both these periodic curves, the circle and figure-eight pattern on the hemisphere, are shown in figure 2. The circle and figure-eight pattern have thereby been placed horizontally, i.e. with an elevation angle $\gamma = \frac{\pi}{2}$ of the direction vector pointing from the center of the sphere to the center of the circle or crossing point of the figure-eight pattern.

A generic (inclined) and oriented version of the small circle of figure 2 on a hemisphere of radius R centered around the origin can be uniquely specified by (half of) the opening angle $0 \leq \theta_\rho \leq \frac{\pi}{2}$, the elevation and azimuthal angle $0 \leq \gamma_c \leq \frac{\pi}{2}$ and $0 \leq \psi_c \leq 2\pi$, respectively, and the orientation $\sigma = \pm 1$. The angles define the circle radius $0 \leq R_c \leq R$ and a unit vector as

$$R_c = R \sin \theta_\rho , \quad \vec{e}_{r_c} = \begin{pmatrix} \sin \theta_c \cos \psi_c \\ \sin \theta_c \sin \psi_c \\ -\cos \theta_c \end{pmatrix} , \quad \theta_c = \frac{\pi}{2} - \gamma_c . \quad (3)$$

The vector is given in the north-east-down (NED) coordinate system of avionics, where vectors with positive third components point downwards. Geometrically, on a hemisphere with radius R the above data describes a circle of radius R_c that is embedded in the plane perpendicular to \vec{e}_{r_c} , i.e. it is i.e. rotated by ψ_c to the east and

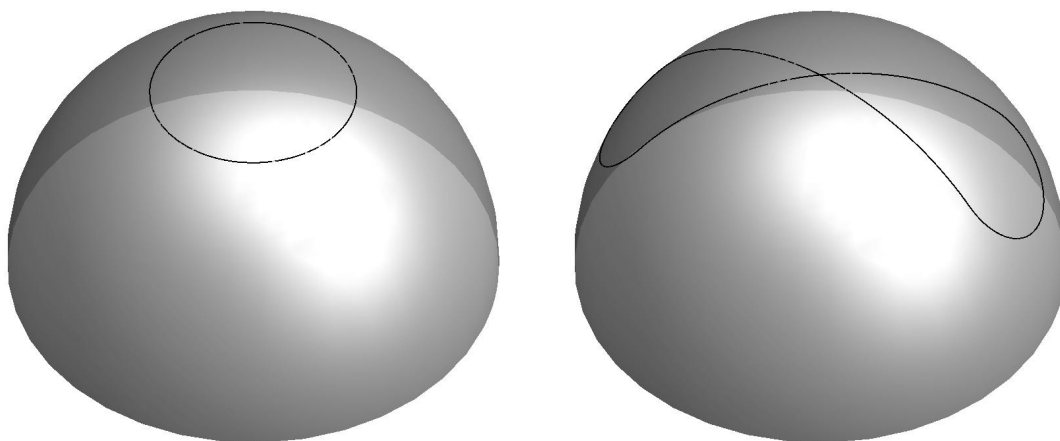


Figure 2: Small circle and figure-eight pattern as simple periodic flight paths on a hemisphere for elevation $\gamma = 45^\circ$.

inclined by γ_c towards the sky and located at a distance

$$D = R \cos \theta_\rho \quad (4)$$

from the ‘home’ position. Hence, the intersection of the plane at the above given distance with the hemisphere yields the circle. The vector \vec{r}_c from the ‘home’ position to the center of the circle is given by

$$\vec{r}_c = D\vec{e}_{r_c} . \quad (5)$$

The orientation of the circle is fixed by applying in the case $\sigma = +1$ the right hand rule along the rotated z -axis of the NED coordinate system, i.e. along $-\vec{r}_c$. Hence, circles with $\sigma = +1$ and $\sigma = -1$ are oriented clockwise and counterclockwise when observed from above, respectively. In this convention, the orientation yields the sign for the roll angle of an upright-oriented aircraft³ following the circular path in accord with its orientation.

An oriented circle segment of a small circle on a hemisphere of radius R can be uniquely specified by (half of) the opening angle θ_ρ defining the circle radius via (3), four angles, given as before by the elevation γ_c and azimuthal angle ψ_c as well as $0 < \phi_i < 2\pi$, $i = 1, 2$. The angles ϕ_1 and ϕ_2 determine the start- and endpoint of the circle segment around \vec{e}_{r_c} . They are the angles of polar coordinates in a coordinate system on the plane with normal vector (3). For angles that increase in the direction determined by the right hand rule applied to $-\vec{e}_{r_c}$, the orientation is then given by $\sigma = \text{sgn}(\phi_2 - \phi_1)$. Alternatively, if $\phi_2 - \phi_1 \neq n\pi$, $n \in \mathbb{Z}$, the oriented circle segment may be defined by substituting in (3) the unit vector \vec{e}_{r_c} by an ordered set of two unitvectors $\vec{e}_{t,i} = \vec{e}_t(\phi_i)$, $i = 1, 2$ that are the tangent vectors at the start and end point, respectively. The unit normal vector \vec{e}_{r_c} pointing into the ‘upper’ hemisphere

³Here, upright-oriented means that the projection of the down direction of the aircraft-fixed coordinate system onto the down direction of the NED coordinate system is non-negative.

towards the center of the circle segment is then obtained as

$$\vec{e}_{rc} = -\frac{\vec{e}_{t,1} \times \vec{e}_{t,2}}{\sin(\phi_2 - \phi_1)}. \quad (6)$$

At a generic position $\vec{r}(\phi)$ on the circle segment parameterized by $\phi_{\min} \leq \phi \leq \phi_{\max}$, $\phi_{\min} = \min(\phi_1, \phi_2)$, $\phi_{\max} = \max(\phi_1, \phi_2)$, the tangent space of the sphere, which is a plane, contains the tangent vector $\vec{e}_t(\phi)$ of the curve. The direction normal to the sphere and the tangent plane are spanned by the unit vectors

$$\vec{e}_r(\phi) = \frac{\vec{r}(\phi)}{|\vec{r}(\phi)|}, \quad \vec{e}_{p,1}(\phi) = \vec{e}_t(\phi), \quad \vec{e}_{p,2}(\phi) = \vec{e}_r(\phi) \times \vec{e}_{p,1}(\phi). \quad (7)$$

The decomposition of the curvature κ of a curve on the sphere into the geodesic curvature κ_g associated with the projection of the curve onto the tangent plane of the sphere and the normal curvature κ_n read

$$\frac{\partial_\phi \vec{e}_t(\phi)}{|\partial_\phi \vec{r}(\phi)|} = \kappa(\phi) \vec{e}_n(\phi) = \kappa_g(\phi) \vec{e}_{p,2}(\phi) + \kappa_n \vec{e}_r(\phi), \quad \kappa_n = -\frac{1}{R}, \quad (8)$$

where $\vec{e}_n(\phi)$ is the normal vector of the curve.⁴ For a circle segment, $\kappa = \frac{1}{R_c}$ is constant, and the geodesic curvature reads with the definition of θ_ρ in (4)

$$\kappa_g = \frac{\sqrt{R^2 - R_c^2}}{RR_c} = \frac{\cot \theta_\rho}{R}. \quad (9)$$

In the special case $\theta_\rho = \frac{\pi}{2}$, the geodesic curvature is zero, indicating that the resulting circle segment is a geodesic, i.e. a great circle segment. Indeed, the plane defined via (4) and (5) then contains the center point of the hemisphere since $D = 0$ and thus yields a great circle segment.

The oriented figure-eight pattern shown in figure 2 can be constructed from four oriented circle segments, of which two are great circle segments and two are small circle segments. The two great circle segments are of equal length and intersect each other at half of their length. The intersection is called the crossing point of the figure-eight pattern. Each pair of neighbored endpoints is connected via a small circle. If the plane defining this small circle contains the respective two endpoints of the great circles and is spanned by the tangent vectors of the great circles at these points, the piecewise defined curve is C^1 at the connections.

In the NED coordinate system, the figure-eight pattern is most easily constructed at the pole of the ‘upper’ hemisphere with an orientation from east to west. The

⁴Here, $\vec{e}_n(\phi)$ is defined such that $\kappa(\phi) \geq 0$ and therefore is not the outer normal vector but points into the direction into which the curve deviates from a straight line, which for a circle is the interior. Hence, (8) differs by a sign from (27) which is formulated for the outer normal vector.

location of the crossing point and vectors pointing towards the centers of the eastern ($\sigma_e = +1$) and western ($\sigma_e = -1$) turning circles according to (3) are then given by

$$\vec{r}_0 = R \begin{pmatrix} 0 \\ 0 \\ -1 \end{pmatrix}, \quad \vec{e}_{r_c, \sigma_e} = \begin{pmatrix} 0 \\ \sigma_e \sin \theta_c \\ -\cos \theta_c \end{pmatrix}, \quad (10)$$

where $\theta_c \geq \theta_\rho$ is required in order to avoid multiple self intersections. For an orientation $\sigma = +1$ of the figure-eight pattern, the eastern and western turning circles are oriented clockwise and counter clockwise when observed from above, respectively. Their orientations are then given by σ_e .

The two geodesic segments that intersect in \vec{r}_0 at an angle $0 < \chi_0 \leq \pi$ are parameterized as

$$\vec{r}_{g\pm}(\theta) = R \begin{pmatrix} \pm \sin \theta \sin \frac{\chi_0}{2} \\ \sin \theta \cos \frac{\chi_0}{2} \\ -\cos \theta \end{pmatrix}, \quad -\theta_t \leq \theta \leq \theta_t, \quad (11)$$

where θ_t is the polar angle at the two eastern endpoints of the two geodesic segments. At these points and their two western counterparts, the transgressions between the segments occur, and we will hence from now on denote them as transgression points. The projection of $\vec{r}_{g\pm}(\theta_t)$ onto the direction $\vec{e}_{r_c, +}$ of the eastern turning circle center yields

$$\frac{\vec{r}_{g,\pm}(\theta_t) \cdot \vec{e}_{r_c, +}}{R} = (\sin \theta_t \sin \theta_c \cos \frac{\chi_0}{2} + \cos \theta_t \cos \theta_c) = \cos \theta_\rho. \quad (12)$$

The unit tangential vectors at the north-eastern, north-western, south-eastern, south-western transgression points labeled by $(\sigma_n, \sigma_e) = (+, +), (+, -), (-, +), (-, -)$ and the two required cross products read

$$\vec{e}_{t, \sigma_n, \sigma_e} = \begin{pmatrix} \cos \theta_t \sin \frac{\chi_0}{2} \\ \sigma_n \sigma_e \cos \theta_t \cos \frac{\chi_0}{2} \\ \sigma_n \sin \theta_t \end{pmatrix}, \quad \sigma_e \vec{e}_{t, +, \sigma_e} \times \vec{e}_{t, -, \sigma_e} = 2 \cos \theta_t \sin \frac{\chi_0}{2} \begin{pmatrix} 0 \\ \sigma_e \sin \theta_t \\ -\cos \theta_t \cos \frac{\chi_0}{2} \end{pmatrix}. \quad (13)$$

The latter expression has to be parallel to \vec{e}_{r_c, σ_e} in (10), and this determines the polar angle of the eastern center point direction as

$$\tan \theta_c = \frac{\tan \theta_t}{\cos \frac{\chi_0}{2}}. \quad (14)$$

The relations (12) and (14) determine θ_t and χ_0 in terms of the given angles θ_c and θ_ρ as

$$\cos \theta_t = \frac{\cos \theta_c}{\cos \theta_\rho}, \quad \cos \frac{\chi_0}{2} = \frac{\sqrt{\sin^2 \theta_c - \sin^2 \theta_\rho}}{\sin \theta_c}. \quad (15)$$

The position vectors of the four transgression points and their tangential vectors determining the orientation of the segments and outer normal vectors are then expressed as functions of θ_c and θ_ρ as

$$\begin{aligned}\vec{r}_{g,\sigma_n,\sigma_e} &= \frac{R}{\cos\theta_\rho \sin\theta_c} \begin{pmatrix} \sigma_n \sin\theta_\rho \sqrt{\sin^2\theta_c - \sin^2\theta_\rho} \\ \sigma_e(\sin^2\theta_c - \sin^2\theta_\rho) \\ -\sin\theta_c \cos\theta_c \end{pmatrix}, \\ \vec{e}_{t,\sigma_n,\sigma_e} &= \frac{1}{\cos\theta_\rho} \begin{pmatrix} \sin\theta_\rho \cot\theta_c \\ \sigma_n \sigma_e \cot\theta_c \sqrt{\sin^2\theta_c - \sin^2\theta_\rho} \\ \sigma_n \sqrt{\sin^2\theta_c - \sin^2\theta_\rho} \end{pmatrix}, \\ \vec{e}_{n,\sigma_n,\sigma_e} &= \sigma_e \vec{e}_{r_c,\sigma_e} \times \vec{e}_{t,\sigma_n,\sigma_e} = \frac{1}{\cos\theta_\rho \sin\theta_c} \begin{pmatrix} \sigma_n \sqrt{\sin^2\theta_c - \sin^2\theta_\rho} \\ -\sigma_e \sin\theta_\rho \cos^2\theta_c \\ -\sin\theta_\rho \sin\theta_c \cos\theta_c \end{pmatrix}.\end{aligned}\tag{16}$$

The angle ϕ_c swept by each small circle segment is determined as

$$\sin\frac{\phi_c}{2} = \sqrt{\frac{1 + \vec{e}_{t,+,\sigma_e} \cdot \vec{e}_{t,-,\sigma_e}}{2}} = \frac{\tan\theta_\rho}{\tan\theta_c}.\tag{17}$$

According to (4) and(5), the two center points of the turning circles and apices of the figure-eight pattern are located at

$$\vec{r}_{c,\sigma_e} = R \cos\theta_\rho \begin{pmatrix} 0 \\ \sigma_e \sin\theta_c \\ -\cos\theta_c \end{pmatrix}, \quad \hat{r}_{\sigma_e} = \vec{r}_{c,\sigma_e} + R \sin\theta_\rho \begin{pmatrix} 0 \\ \sigma_e \cos\theta_c \\ \sin\theta_c \end{pmatrix} = R \begin{pmatrix} 0 \\ \sigma_e \sin\hat{\theta} \\ \cos\hat{\theta} \end{pmatrix},\tag{18}$$

where (half of) the maximum swept polar angle is given by

$$\hat{\theta} = \theta_c + \theta_\rho.\tag{19}$$

Clearly, to stay on the ‘upper’ hemisphere, one has to choose θ_c and θ_ρ such that $\hat{\theta} \leq \frac{\pi}{2}$.

The figure-eight pattern with a generic azimuthal and elevation angle such that the crossing point \vec{r}_0 in (10) is transformed to $\vec{r}_0 = (\sin\theta_0 \cos\psi_0, \sin\theta_0 \sin\psi_0, -\cos\theta_0)^t$ can be obtained by applying a rotation $R(\theta_0, \psi_0)$. The orientation of the figure-eight pattern should always be horizontal, i.e. the two turning points should always have the same z -coordinate. This can be achieved by first performing an active rotation with angle $-\theta_0$ around the y -axis. Then, one performs an active rotation with angle ψ_0 around the z -axis.

The rotation matrix that combines two such active rotations but with angles given by $-\theta$ and ψ , reads

$$R(\theta, \psi) = (\vec{e}_\theta, \vec{e}_\psi, -\vec{e}_r),\tag{20}$$

where vectors in the directions of the north, east, down axes are mapped to

$$\vec{e}_\theta = \begin{pmatrix} \cos \theta \vec{e}_1 \\ \sin \theta \end{pmatrix}, \quad \vec{e}_\psi = \begin{pmatrix} \vec{e}_2 \\ 0 \end{pmatrix}, \quad \vec{e}_r = \begin{pmatrix} \sin \theta \vec{e}_1 \\ -\cos \theta \end{pmatrix}, \quad (21)$$

respectively. The basis vectors in the lateral (north-east) subspace are given by

$$\vec{e}_1 = \begin{pmatrix} \cos \psi \\ \sin \psi \end{pmatrix}, \quad \vec{e}_2 = \begin{pmatrix} -\sin \psi \\ \cos \psi \end{pmatrix}. \quad (22)$$

With $\theta_0 = \frac{\pi}{2} - \gamma_0$, the oriented figure-eight is hence specified by its

$$\begin{aligned} \text{shape:} & \quad 0 < \theta_c < \frac{\pi}{2}, & \quad 0 < \theta_\rho \leq \theta_c, & \quad \theta_c + \theta_\rho \leq \frac{\pi}{2}, \\ \text{attitude:} & \quad 0 \leq \gamma_0 \leq \frac{\pi}{2}, & \quad 0 \leq \psi_0 \leq 2\pi, \\ \text{orientation:} & \quad \sigma = \pm 1. \end{aligned} \quad (23)$$

2.3 Navigation and control strategy

The navigation of the aircraft is divided into lateral (NE subspace) navigation and speed-height control. The navigation controller determines the demanded lateral acceleration of the aircraft and computes the demanded roll angle from it. Furthermore, the demanded height is transferred to the speed-height-controller. This control strategy requires the decomposition of the desired flight path into lateral and height components.

The small circle defined via (3) can be parameterized in terms of the time-dependent angle $0 \leq \phi(t) < 2\pi$. For $0 < \theta_c < \frac{\pi}{2}$, the vector \vec{e}_1 shall point from the lateral projection of the center point of the circle to that of the initial point on the circle where $\phi = 0$.⁵ This parameterization together with the resulting velocity reads

$$\begin{aligned} \vec{r}(\phi) &= R(\cos \theta_\rho \vec{e}_{r_c} + \sin \theta_\rho (\cos \phi \vec{e}_{\theta_c} + \sigma \sin \phi \vec{e}_{\psi_c})), \\ \dot{\vec{r}}(\phi) &= -v_c(\sin \phi \vec{e}_{\theta_c} - \sigma \cos \phi \vec{e}_{\psi_c}), \quad v_c = R\dot{\phi} \sin \theta_\rho, \end{aligned} \quad (24)$$

where the occurring unit vectors are the ones of (21) with angles θ_c, ψ_c . This parameterization decomposes into the lateral and height direction as

$$\begin{aligned} \vec{r}_1(\phi) &= R(\cos \theta_\rho \sin \theta_c \vec{e}_1 + \sin \theta_\rho (\cos \phi \cos \theta_c \vec{e}_1 + \sigma \sin \phi \vec{e}_2)), \\ z(\phi) &= -R(\cos \theta_\rho \cos \theta_c - \cos \phi \sin \theta_\rho \sin \theta_c), \\ \dot{\vec{r}}_1(\phi) &= -v_c(\sin \phi \cos \theta_c \vec{e}_1 - \sigma \cos \phi \vec{e}_2), \\ \dot{z}(\phi) &= -v_c \sin \phi \sin \theta_c. \end{aligned} \quad (25)$$

The unit tangent and outer normal vector in the lateral plane obtained from the above parameterization read

$$\vec{e}_{t1}(\phi) = -\frac{\sin \phi \cos \theta_c \vec{e}_1 - \sigma \cos \phi \vec{e}_2}{\sqrt{\cos^2 \phi + \sin^2 \phi \cos^2 \theta_c}}, \quad \vec{e}_{n1}(\phi) = \frac{\cos \phi \vec{e}_1 + \sigma \sin \phi \cos \theta_c \vec{e}_2}{\sqrt{\cos^2 \phi + \sin^2 \phi \cos^2 \theta_c}}. \quad (26)$$

⁵For $\theta_c = 0$, we choose \vec{e}_1 to point into the northern direction.

They determine the lateral curvature κ_l as

$$\frac{\partial_\phi \vec{e}_{tl}(\phi)}{|\partial_\phi \vec{r}_l(\phi)|} = -\kappa_l(\phi) \vec{e}_{nl}(\phi), \quad \kappa_l(\phi) = \frac{\cos \theta_c}{R \sin \theta_\rho \sqrt{\cos^2 \phi + \sin^2 \phi \cos^2 \theta_c}}. \quad (27)$$

It enters the expression for the centripetal acceleration that is required in order to stay on the given curve

$$a_l(\phi) = v_l(\phi)^2 \kappa_l(\phi) = \frac{v_c^2}{R \sin \theta_\rho} \frac{\cos \theta_c}{\sqrt{\cos^2 \phi + \sin^2 \phi \cos^2 \theta_c}}, \quad (28)$$

where the lateral velocity is determined from (25) as

$$v_l(\phi) = |\dot{\vec{r}}_l(\phi)| = v_c \sqrt{\cos^2 \phi + \sin^2 \phi \cos^2 \theta_c}. \quad (29)$$

In order to follow the desired flight path, the controller has to compare the measured with the desired position and attitude. The distance of the measured position from the desired flight path and also the deviation of the flight direction from the tangential direction at the corresponding location on the flight path have to be determined. Let \vec{r}_a and \vec{v}_a be the measured position and velocity of the aircraft, respectively. The position vector \vec{r}_p of the closest point on the circle is given by

$$\vec{r}_p = D \vec{e}_{rc} + R \sin \theta_\rho \vec{e}_{np}, \quad (30)$$

where the tangent vector and outer normal vector at the position \vec{r}_p on the circle read

$$\vec{e}_{tp} = \sigma \frac{\vec{r}_a \times \vec{e}_{rc}}{|\vec{r}_a \times \vec{e}_{rc}|}, \quad \vec{e}_{np} = \sigma \vec{e}_{rc} \times \vec{e}_{tp} = \frac{\vec{r}_a - (\vec{r}_a \cdot \vec{e}_{rc}) \vec{e}_{rc}}{\sqrt{r_a^2 - (\vec{r}_a \cdot \vec{e}_{rc})^2}}, \quad (31)$$

and they obey $\vec{e}_{tp} \times \vec{e}_{np} = \sigma \vec{e}_{rc}$. The decomposition into lateral direction and height requires their normalized lateral projections and the outer normal vector

$$\vec{e}_{tpl} = \frac{\vec{e}_{tp} - e_{tp,3} \vec{e}_3}{\sqrt{1 - e_{tp,3}^2}}, \quad \vec{e}_{rpl} = \frac{\vec{e}_{np} - e_{np,3} \vec{e}_3}{\sqrt{1 - e_{np,3}^2}}, \quad \vec{e}_{npl} = \sigma \frac{\vec{e}_{tp} \times \vec{e}_3}{\sqrt{1 - e_{tp,3}^2}}. \quad (32)$$

While \vec{e}_{npl} has been constructed such that $\vec{e}_{tpl} \cdot \vec{e}_{npl} = 0$, this is not the case for \vec{e}_{rpl} . In fact, unlike for the inclined circle, for an ellipse which is its lateral projection, the lateral radial and normal vector are not parallel at a generic position. Their inner product reads

$$\vec{e}_{rpl} \cdot \vec{e}_{npl} = \frac{|e_{rc,3}|}{\sqrt{(1 - e_{tp,3}^2)(1 - e_{np,3}^2)}}. \quad (33)$$

The result for the lateral acceleration (28) can be obtained even without knowing the value of ϕ at the location \vec{r}_p . From (26) it follows that

$$a_l = \frac{v_c^2}{R \sin \theta_\rho} \sqrt{\cos^2 \theta_c (\vec{e}_1 \cdot \vec{e}_{npl})^2 + (\vec{e}_2 \cdot \vec{e}_{npl})^2}. \quad (34)$$

The deviation of the measured from the desired position, its lateral projection and its component in normal direction read

$$\vec{r}_{pa} = \vec{r}_a - \vec{r}_p, \quad \vec{r}_{pal} = \vec{r}_{pa} - r_{pa,3}\vec{e}_3, \quad \delta r_1 = \text{sgn}(\vec{r}_{pal} \cdot \vec{e}_{npl})|\vec{r}_{pal}|, \quad h = -r_{p,3}, \quad (35)$$

where we have also indicated the demanded height that is transferred to the speed-height controller. Note that δr_1 is not the distance of the aircraft's position from the ellipse, since the lateral projection of the nearest point on the circle does in general not yield the nearest point on the resulting ellipse. It can nevertheless be used as a measure of the deviation from the desired flight path.

The lateral projection of the velocity vector and its component in normal direction read

$$\vec{v}_{pal} = \vec{v}_a - v_{a,3}\vec{e}_3, \quad \delta v_1 = \vec{v}_{pal} \cdot \vec{e}_{npl}. \quad (36)$$

The acceleration that has to be provided by the appropriate roll angle reads

$$a = a_1 + K_r \delta r_1 + K_v \delta v_1, \quad (37)$$

where K_r and K_v are positive gains of the proportional and differential feedback that yield the PD-controller, respectively.

The roll angle Φ is determined from the equilibrium of the centripetal, lift and gravitational forces acting on the aircraft. Considering a pitch angle Θ , the result reads

$$\Phi = \sigma \arctan \frac{a \cos \Theta}{g}, \quad -\frac{\pi}{2} \leq \Phi \leq \frac{\pi}{2}. \quad (38)$$

The tether force (2) is not considered in the calculation of Φ .

2.4 Code for fixed-wing aircraft

For a fixed-wing aircraft, the vehicle specific code of the `ardupilot` autopilot is denoted as `ArduPlane`. In the following, it is described how flight modes are embedded in this code. The new flight modes for tethered flight along rotated and inclined circles and figure-eight patterns are called `LOITER_3D` and `EIGHT_SPHERE`, respectively.

The main file of the code for fixed-wing aircraft is `ArduPilot.cpp` with its header `Plane.h`. It contains the list of tasks called `scheduler_tasks`. In the main loop function `loop()`, these tasks are executed after a sample has been obtained from the sensors. It runs at a rate `_loop_rate_hz=400Hz`, i.e. every `loop_us=2500μs`. The tasks run at individual rates, i.e. not each task is due to run in each main loop cycle. The tasks of immediate relevance for navigation are shown in figure 3 in the box labeled `ArduPlane.cpp`. The list is causally ordered, and this order does not necessarily coincide with the temporal order in which the individual tasks are executed by the scheduler.

First, `ahrs_update` calls the `update()` method from the attitude and height reference system `AHRS` class. It uses an extended Kalman filter (EKF) to fuse the sensor data in order to determine the state of the aircraft, e.g its position and attitude. The

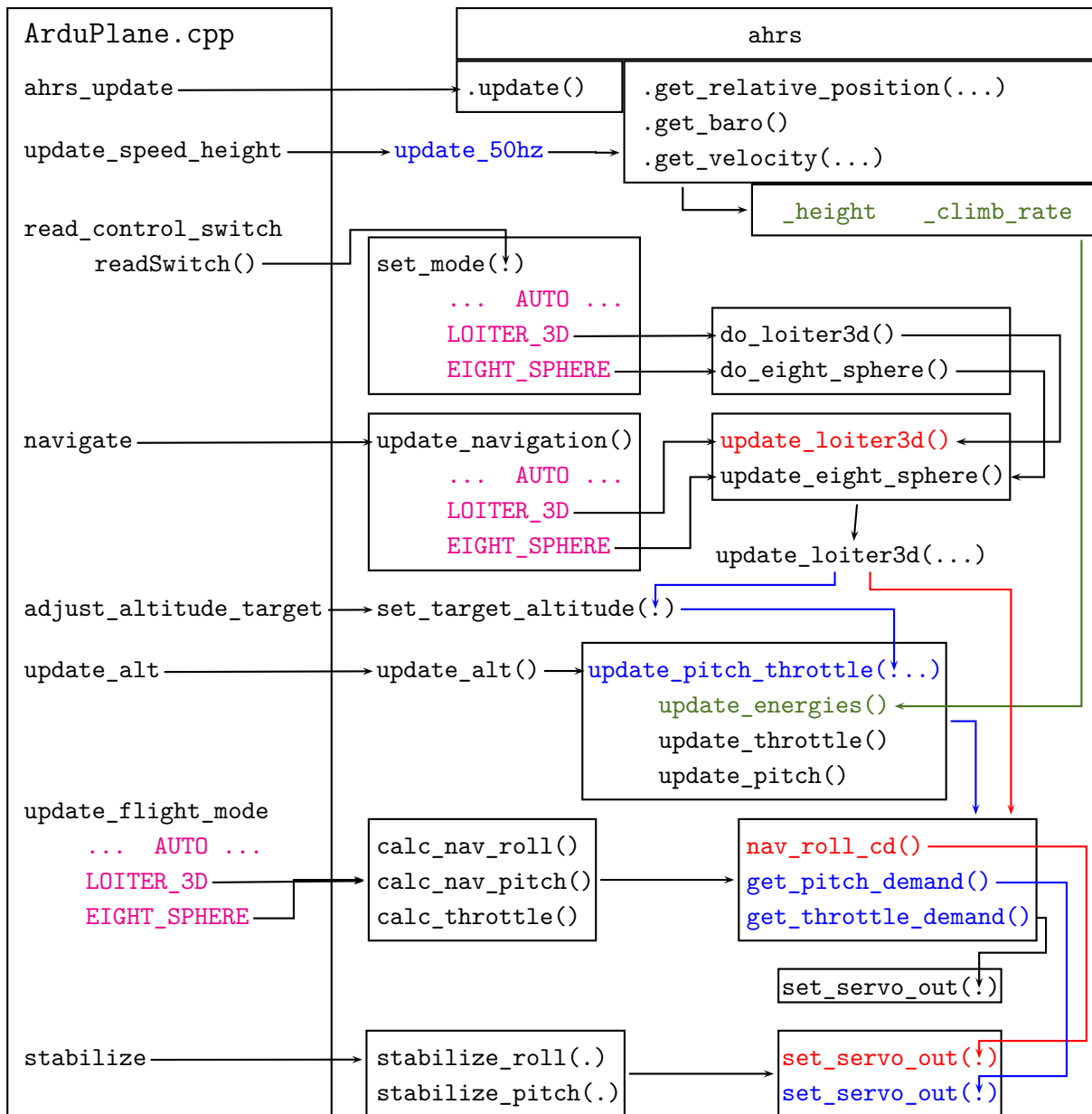


Figure 3: Embedding of the new flight modes `LOITER_3D` and `EIGHT_SPHERE` into the ardupilot code for fixed-wing aircraft (ArduPlane). Speed and height are controlled by the *total energy control system (TECS)*. Lateral navigation is provided by an *L1-controller* [33] in case of straight flight paths or a *PD-controller* in case of circles or circle segments.

task `update_speed_height` then reads that data with respective methods of the `ahrs` object and stores the calculated height and climb rate in the variables `_height` and `_climb_rate`, respectively. The task `read_control_switch` selects the flight mode according to the positions of the control switches of the RC transmitter or GCS. In figure 3, some of these modes are shown and highlighted in magenta. The mode `AUTO` navigates along a polygon given in terms of corner points (waypoints). The modes for tethered flight are `LOITER_3D` and `EIGHT_SPHERE`. They implement the flight along given rotated and inclined versions of the circle and figure-eight pattern shown in

figure 2, respectively. The selected flight mode is initialized when the corresponding control switch is activated. For the modes `LOITER_3D` and `EIGHT_SPHERE` this happens by calling `do_loiter3d()` and `do_eight_sphere()`, respectively. Then, the task `navigate` calls the virtual function `update_loiter3d()` or `update_eight_sphere()`. Via dynamic binding they call their counterparts defined in the selected navigation controller class which is `A_L1_control`. In the `LOITER_3D` case, the called function is `update_loiter3d(...)` that takes certain parameters as its argument, calculates the demanded height given in (35) and employs a PD-controller to calculate the demanded lateral acceleration given in (37). In the `EIGHT_SPHERE` case, `update_eight_sphere()` selects the current segment of the figure-eight pattern in dependence of the current position of the aircraft. Then, it calls `update_loiter3d(...)` of the `A_L1_control` class with the parameters of the selected segment. The demanded height (35) is then transferred via the function `set_target_altitude` of the task `adjust_altitude_target` to the total energy control system (TECS) that is called from the task `update_alt`. It calculates the desired pitch and throttle from the demanded height and the measured `_height` and `_climb_rate`. The task `update_flight_mode` then calculates the roll angle from the accelerations according to (38) in `nav_roll_cd()` and simply reads out the pitch and throttle demand that were determined by the TECS. Moreover, it transfers the throttle demand to the servos via the function `set_servo_out`. The task `stabilize` then also transfers the required roll and pitch angle to the servos.

3 Simulation

We have tested the modes for tethered flight in simulations. This is recommended in order to debug the code and to reduce the risk of malfunction in real tests. The autopilot `ardupilot` admits compilation for a SITL environment. It uses the flight dynamics model `JSBSim` with `MAVProxy` as GCS. The models of aircraft are already included in the simulation software. The default model is for the Rascal 110, which is used for the tests of the tethered flight modes. The various coefficients and characteristics of the aircraft model are specified in several files via the extended markup language (XML). In particular, it is possible to add external forces acting on the aircraft in specified directions at specified positions. A model for the tether force can be implemented in this way. We have added it to the aircraft model as `<external_reactions>` that acts at the center of mass of the aircraft in the direction of the unit vector pointing from that point to the ‘home’ location. The strength of the force depends on the distance from ‘home’ as given in (2). So far, we have not implemented a model of our test platform, i.e. of the modified Easy Star II. But even without such a model the SITL environment was invaluable for debugging the code and for ensuring that our aircraft can be safely operated in the flight tests described below.

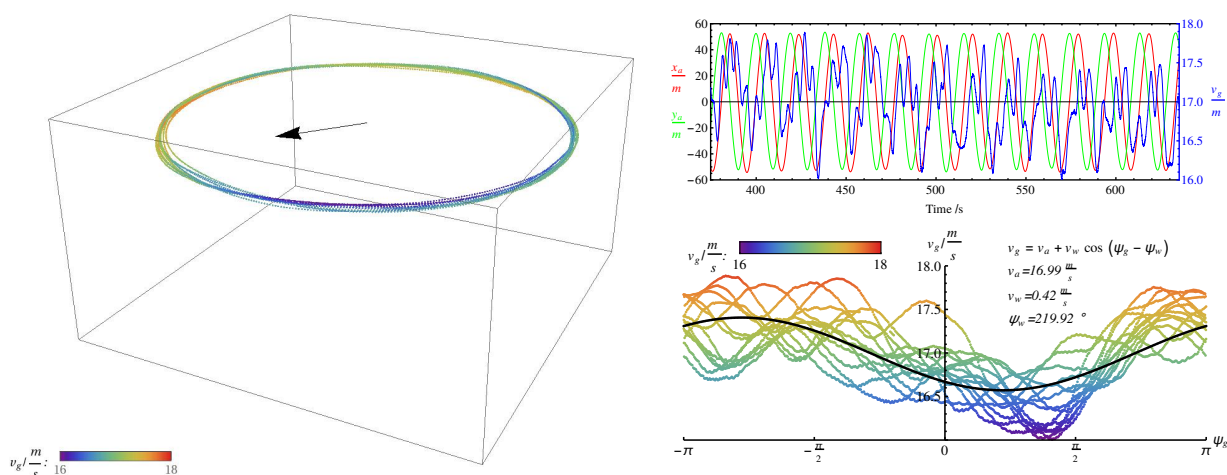


Figure 4: Circular path used for the calibration of the airspeed sensor. The ground speed v_g is encoded by the color and the determined wind direction is shown. The time-dependence of the measured lateral position and ground speed velocity as well as the fit to the data is shown on the rhs.

4 Flight tests and data analysis

In this section, we analyze the data from our flight tests. The tests start with a flight of a horizontal circle at fixed altitude without tether in order to calibrate the airspeed sensor and to determine the wind direction and speed. Then, the aircraft is ready for testing the tethered flight modes.

The autopilot stores the system status and state as well as environmental data into several log files. One of these contains the data as lines of comma separated values (CSV) in temporal order of which the first entry of each line is an identifier of the source of information. For each identifier the format as well as type of its data is specified in the preamble. For instance, the identifiers NKF1 to NKF4 contain information for the first extended Kalman filter (EKF) instance [34]. The following analysis relies mainly on the NKF1 line that contains attitude, position, ground speed data of the aircraft and on the AHRS line that contains the measured airspeed. Moreover, the CTUN line is used to retrieve information about the throttle. Thereby, data from different sources such as e.g. the position from NKF1 and the airspeed from AHRS has to be combined. This data is logged at different time instances and with different frequencies. We searched for that instance of the desired data logged with the higher frequency (NKF1) that occurs immediately before an instance of the desired data logged with the lower frequency (AHRS or CTUN) and combined them. Since they do not occur at coincident times, we checked that their time differences are small enough to be negligible.

4.1 Calibration of the airspeed sensor

The airspeed sensor measures the airspeed via a Pitot tube that is mounted at the nose of the aircraft as shown in figure 1. It has to be calibrated in order to provide reliable results for the airspeed. To this purpose the aircraft flies along a horizontal circle

several times, keeping constant the airspeed v_a , where we have demand $v_a = 17 \frac{\text{m}}{\text{s}}$. Since the ground speed v_g is determined by the Kalman filter from the measured accelerations and GPS positions, the relation

$$\vec{v}_g = \vec{v}_a + \vec{v}_w \quad (39)$$

can be used to determine v_a and the average wind speed v_w and wind direction ψ_w in the NED coordinate system from the time series of data points. If $v_w \ll v_g, v_a$ as in the present case, \vec{v}_g and \vec{v}_a , almost point into the same direction. The above relation then simplifies for a circular flight path defined via (3) with $\gamma = 90^\circ$ the following relation for the lateral components

$$(v_g - v_a) \begin{pmatrix} \cos \psi_g \\ \sin \psi_g \end{pmatrix} = v_w \begin{pmatrix} \cos \psi_w \\ \sin \psi_w \end{pmatrix}, \quad (40)$$

where ψ_g is the angle corresponding to the direction of the ground speed vector. On the considered circular path, \vec{v}_g and the vector pointing radially from the center of the circle to the position of the aircraft are perpendicular. Hence, the two angles corresponding to their directions are related as $\psi_g = \frac{\pi}{2} - \psi_a$, where ψ_a is the angle associated with the radial vector. Contracting both sides of (40) with $(\cos \psi_g, \sin \psi_g)^t$ yields the ground speed as a function of ψ_g

$$v_g(\psi_g) = v_a + v_w \cos(\psi_g - \psi_w). \quad (41)$$

A fit of this function to the measured data determines v_a , v_w and ψ_w . In figure 4, the circular flight path used for the calibration of the airspeed sensor is shown. Its color encodes the value of v_g . Moreover, the time dependence of the lateral position and ground speed as well as the fit of (41) is shown. The result for the airspeed matches the desired airspeed of $v_a = 17 \frac{\text{m}}{\text{s}}$ very well. The wind speed and wind direction are determined to $v_w = 0.42 \frac{\text{m}}{\text{s}}$ and $\psi_w = 219.92^\circ$, respectively. A vector pointing into that direction is also depicted in the graph of the flight path.

4.2 Figure-eight patterns

In order to test the figure-eight pattern, the aircraft has to be launched, brought to the entry point of the figure-eight pattern and it has also to be landed at the end of the test. Thereby, one has to consider that the attached tether constrains the launch and land patterns. The launch, transfer to the pattern entry point and the pattern itself are flown in a fully autonomous way. In the current implementation, the abort from the pattern and the landing procedure are controlled manually. A test flight consists of the mentioned phases, which in figure 5 are highlighted in different colors for one data set. In the following, the quantitative analysis is performed for the figure-eight flight phases.

Two flight paths that contain figure-eight patterns elevated towards south of the NED coordinate system at elevation angles $\gamma = 45^\circ$ and $\gamma = 30^\circ$ have been recorded.

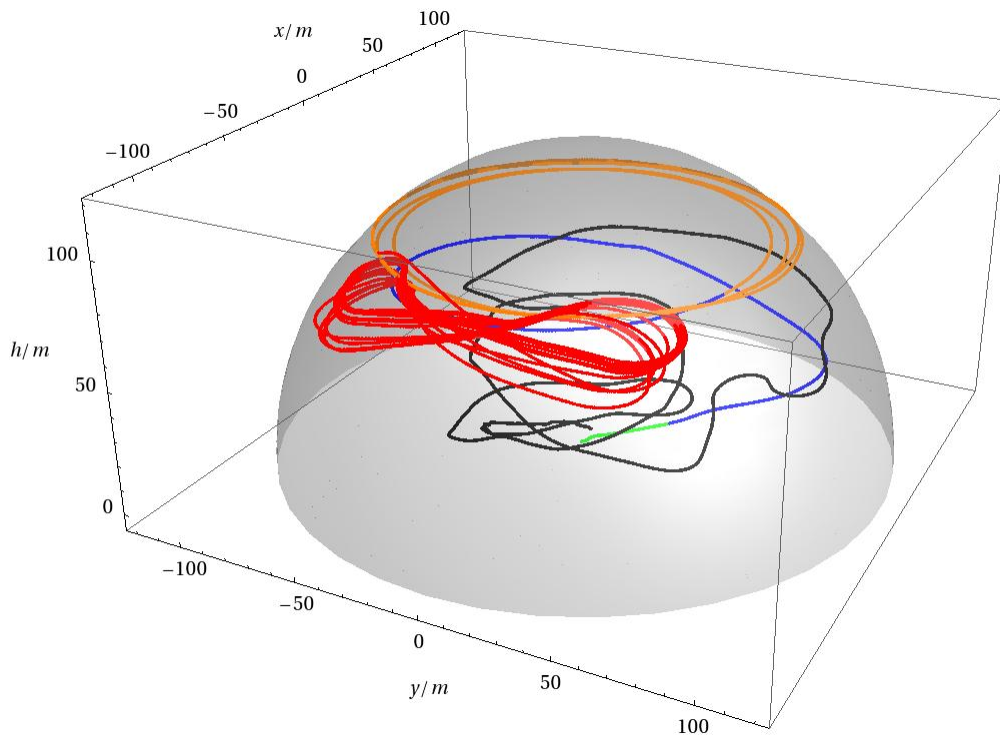


Figure 5: Modes of the tethered test flight. It consists of a launching phase (green), a helix generated by a horizontal circular movement combined with an increment of the altitude (blue), a horizontal circular flight path at the target altitude (orange), the figure-eight pattern (red) and a landing phase (black). All flight phases apart from the manual landing phase are autonomous. Entering and leaving the figure eight-pattern is initiated manually.

They are shown in figure 6 as extracted from the NKF1 entries of the corresponding log files. The shown spheres have radii $R = 120\text{m}$, which is the distance from the ‘home’ position set in the tethered flight modes. In the ideal case of no tether drag that would be the length of the tether. Since the wind velocity was only $v_w = 0.42\frac{\text{m}}{\text{s}}$, the throttle was permanently activated and the aircraft had to be manually landed before it ran out of battery power.

The periodic stationary flights path segments along the two figure-eight patterns are analyzed in the following. They are depicted in red in figure 6. The automatic and manual starting and landing phases, respectively, and also the non-stationary motions in the figure-eight flying mode are depicted in blue.

The attitude of the aircraft is also recorded in the NKF1 entries as the three Euler angles roll (Φ), pitch (Θ) and yaw (Ψ). From these angles, the aircraft-fixed coordinate system can be constructed. In figure 7, it is depicted at some positions of a single figure-eight period. The eastern and western segments of both figure-eight patterns are different. A reasonable explanation of this asymmetry is that the figure-eight patterns are elevated towards south rather than downwind. The downwind location is south-east as evident from figure 4.

Since during the two recorded figure-eight flights the wind speed was very low as also evident from the fit in figure 4, the throttle is automatically activated by

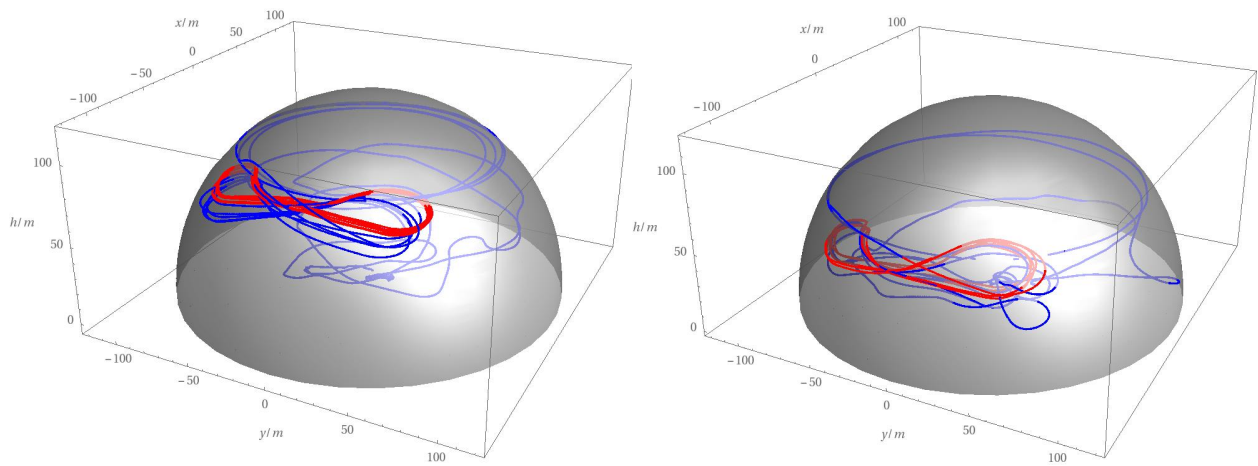


Figure 6: Flight paths with figure-eight pattern elevated towards south at angles $\gamma = 45^\circ$ and $\gamma = 30^\circ$. The stationary figure-eight parts that are analysed in detail are highlighted in red.

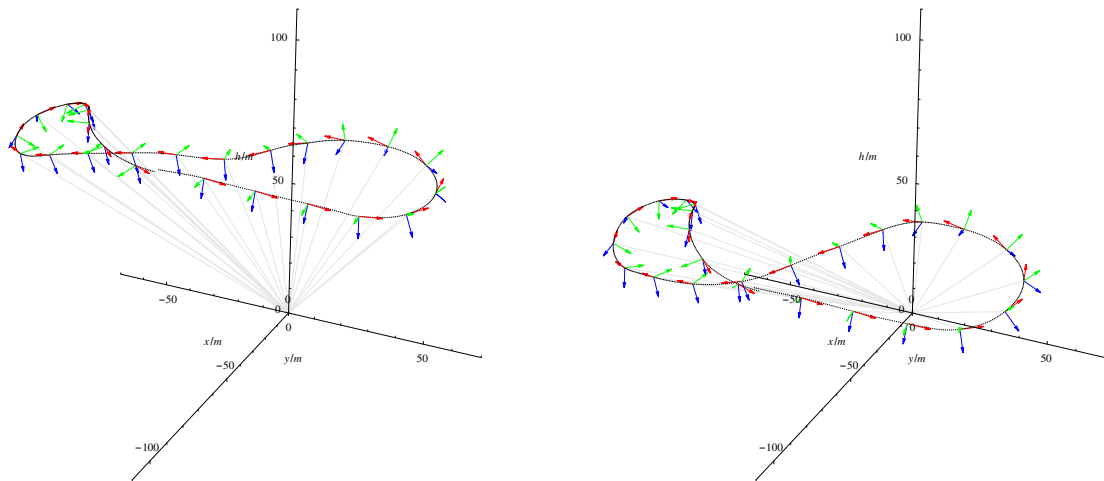


Figure 7: Aircraft-fixed coordinate system at some positions of a single figure-eight period at elevation angles $\gamma = 45^\circ$ and $\gamma = 30^\circ$. The nose, starboard and down axes are depicted in red, green and blue, respectively.

the TECS controller. The time dependence of the throttle and airspeed for both figure-eight patterns at elevation angles $\gamma = 45^\circ$ and $\gamma = 30^\circ$ is shown in figure 8. As can be seen, the throttle is activated whenever the airspeed drops. This periodic behaviour is correlated with the position of the aircraft on the figure-eight pattern. A parameter that captures some of that position information is the angle ψ_a ⁶ between the lateral projections of the two vectors pointing from the center of the sphere to the crossing point and to the aircraft. At the crossing point $\sin \psi_a = 0$ and at the (eastern and western) apices $\sin \psi_a$ assumes its maximum and minimum that depends on the extension of the figure-eight pattern. The airspeed becomes maximal when the

⁶This angle should not be confused with the angle ψ_a introduced in Section 4.1.

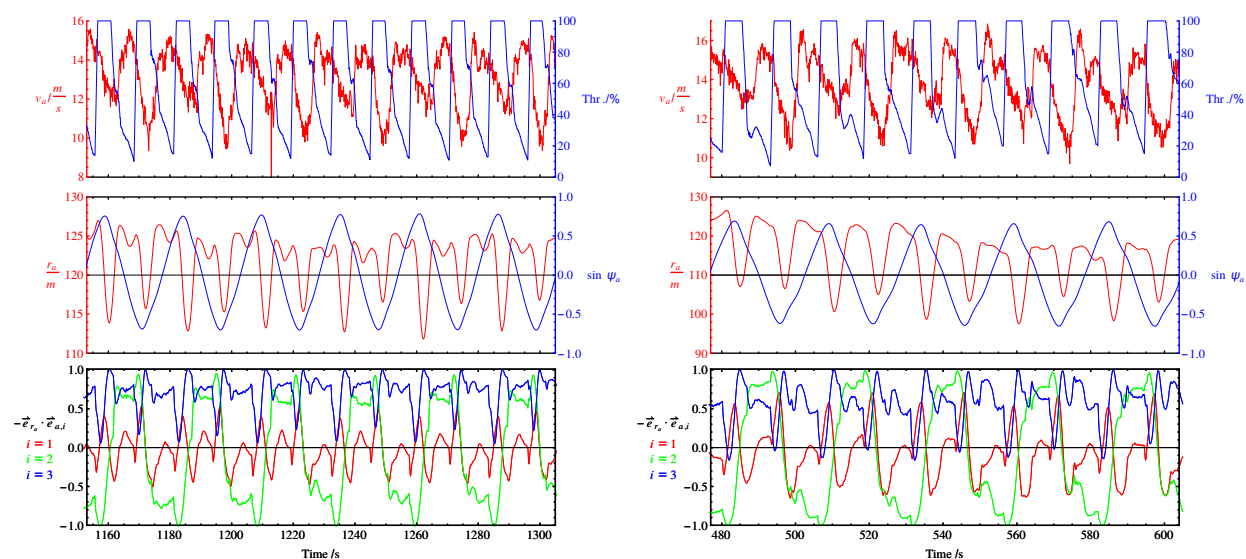


Figure 8: The time dependence of the throttle, airspeed v_a , angle ψ_a between the north direction and the lateral projection of the position vector \vec{r}_a of the aircraft and distance r_a . Time-dependent projections of the aircraft-fixed frame on the direction $-\vec{e}_{r_a}$ pointing to the ‘home’ location. The left and right plots are for the figure-eight patterns at elevation angles $\gamma = 45^\circ$ and $\gamma = 30^\circ$, respectively.

aircraft flies along the geodesic segments, i.e. in an interval around the crossing point. The minima of the airspeed occur approximately at those times where the aircraft reaches one of the two apices, i.e. when it is turning upwards in the turning circles. The airspeed in the eastern and western segment is not symmetric. A reasonable explanation is that the figure-eight pattern is oriented south rather than exactly downwind as evident from the reconstructed wind direction shown in figure 4.

The variation of the airspeed leads to a variation of the lift and drag force. These forces cannot be measured directly. Instead, the tether force could be measured as highly relevant parameter for power generation. However, no force sensor is installed yet. By investigating the variation of the distance r_a of the aircraft from the ‘home’ location one can nevertheless show that the tether is under tension and that this tension depends on the airspeed. The measured distances are also shown in figure 8. One can see that the maxima and minima of the distance follow the maxima and minima of the airspeed. The tether, which runs along a curve due to tether drag, is hence stretched more if the airspeed and hence lift force and tether tension increase. Similar to the airspeed also the distance is not symmetric between the eastern and western figure-eight segments, possibly caused by the fact that the figure-eight pattern is not oriented downwind. The asymmetry could be used to automatically adapt the flight path such that the figure-eight pattern is always oriented downwind.

Next, we analyze the attitude of the aircraft flying along the figure-eight pattern. To this purpose the projections of the three aircraft-fixed axes onto the unit vector $-\vec{e}_{r_a}$ pointing from the position of the aircraft to the ‘home’ position are shown in figure 8 for both figure-eight patterns. The nose-axis is roughly perpendicular to this vector. The maximal deviations occur when the aircraft passes through the apices of

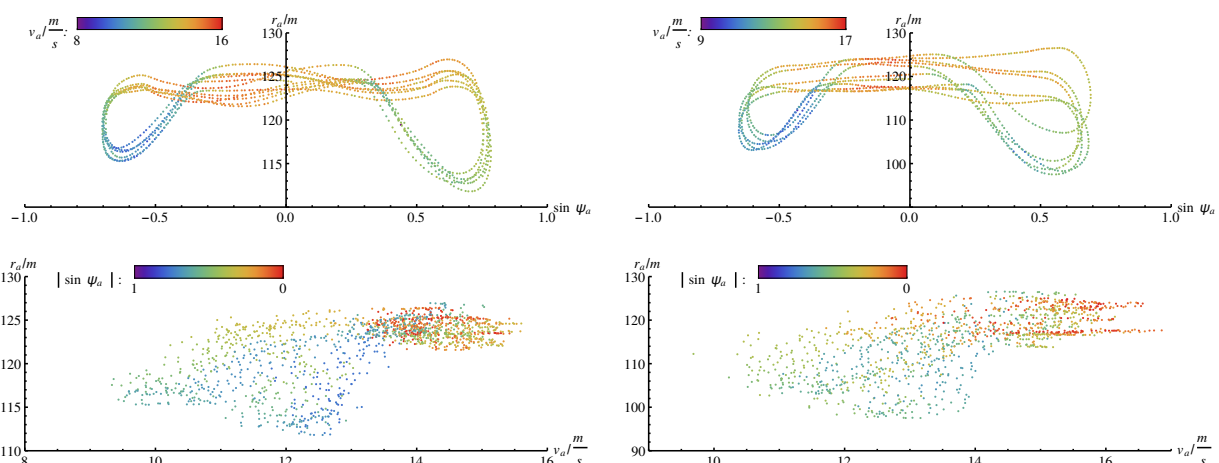


Figure 9: The distance r_a from the aircraft to the ‘home’ location in dependence of the angle ψ_a between the north direction and the lateral projection of \vec{r}_a and the airspeed v_a for the figure-eight patterns at elevation angles $\gamma = 45^\circ$ and $\gamma = 30^\circ$.

the figure-eight pattern. The down-axis is very roughly pointing to the ‘home’ position. The deviations are maximal whenever the projection of the starboard axis onto $-\vec{e}_{r_a}$ is extremal. This projection depends on the roll angle in the tangential frame of the sphere and hence determines the deviation from the geodesic flight path. This deviation should ideally vanish but is found to be not zero when the aircraft passes through the crossing point of the figure-eight pattern. A possible explanation for this deviation is that the attitude of the aircraft has to be such that the gravitational force is compensated. This requires that the aircraft is rotated towards the horizontal attitude more than without the force of gravity. Moreover, the tether force has not been considered so far when the roll angle is determined according to Newton’s law. Especially in strong winds the tether force would dominate the gravitational force and hence should reduce the observed deviation.

Finally, it is very interesting to display the distance r_a as function of the angle ψ_a and of the airspeed v_a . The results are shown in figure 9 for both figure-eight patterns and with v_a or $|\psi_a|$ encoded by the color of the points. The airspeed v_a and the distance r_a are maximal on the geodesic segments, and they are minimal on the turning circles. Moreover, the interval of possible distances that are measured for a given airspeed becomes smaller with increasing airspeed. A reasonable explanation for this is that at higher airspeed and distance the tether is less curved and hence its dynamics has less influence on the system. Moreover, the respective upper limits of r_a are visible as sharp cutoffs. These limits are related to the tether lengths via the unknown tether curve. A model of that curve in the stationary case could be used to estimate their relation. Moreover, the data for the figure-eight pattern elevated at $\gamma = 30^\circ$ suggest that two different tether lengths were used in this flight, since it seems to consist of two copies of a single data set that is shifted along the r_a axis. This is indeed the case, during the flight the tether length was slightly changed by a couple of meters in order to optimize the felt tether force and flight pattern.

5 Conclusions

In this paper we have presented AWESome, our test platform for airborne wind energy systems. It consists of low-cost hardware (for which we spent less than US\$ 1000) and open-source software and hence allows research groups and small startups to test their design strategies without large financial investments. We have demonstrated that an off-the-shelf polystyrene model aircraft with certain reinforcements by carbon fiber fabric can be used as the airborne part of an AWE system in cross-wind flight, where the aircraft is connected to the ground via a tether. We have presented the principal functionality our implementation of two flight modes where the length of the tether is fixed and the aircraft hence moves on a hemisphere. As periodic flight paths we have chosen an inclined circle and a figure-eight pattern. The latter consists of two great and two small circles and hence is based on the algorithms of the former. The SITL environment of the autopilot software enabled us to debug and test our code prior to starting field tests. The results from our real flight tests we have analyzed in detail. This is possible thanks to a complete logging of all sensor and (processed) flight data. While a force sensor for measuring the tether tension is not implemented yet, the results show that the aircraft produces a tether tension that – if scaled up to a larger plane – could in principle be used for power production.

Although our test platform is functional, the current implementation can be extended and improved in many ways. First of all, the figure-eight pattern that consists of four circle segments is only C^1 . The curvature κ and geodesic curvature κ_g are discontinuous at the transgression points of the segments. The roll angle of the aircraft would hence have to be altered infinitely fast to follow that curve. In order to avoid this, the curve should at least be C^2 at all points. For instance, one could implement generalizations of certain sphere-cylinder intersections (Viviani's curves) that are C^∞ and encompass figure-eight patterns.

The separation of the navigation into lateral and speed-height controller appears not to be well suited if an additional force (the tether force) is present and the aircraft moves on a hemisphere. So far, the tether force has not been considered explicitly in the control algorithms. The incorporation of the tether force into the algorithms requires a model for the tether curve or sensors that measure the direction of the tether at the aircraft. In any case a sensor that measures the tether force should be added. The navigation controller could be split into the directions tangential and normal to the sphere at the current position of the aircraft. Our expectation is that this should be advantageous, at least in case of a strong tether force that dominates the gravitational force.

Another interesting area of development is the autonomous adaption of the flight pattern to the wind direction. In [24] one of us has shown that the wind direction can be estimated from the asymmetry of the flight pattern, which in turn can be used to adapt to changing winds. Also, the flight pattern itself could be adapted in real time in order to maximize the power output.

Last but not least, the ground station that so far consists of an offshore fishing

rod should be replaced by a motor driven drum that communicates with the ground station and the aircraft in order to synchronize the release and withdrawal of the tether with the state of the aircraft. The ultimate goal is to construct an automatized launch and landing system.

Concerning further aspects of the test environment, the simulation and data analysis tools could be improved. This concerns the possibility to add tether models to the simulation. Moreover, it would be great to use the flight data in order to extract the aerodynamic coefficients of the real aircraft, that can then be used to set up a more realistic model for the simulation.

We plan to tackle these improvements in the near future. In the meantime, the source code and construction plans of the hard- and software described in this paper are available upon request. We hope that it serves as a basis for close collaborations with the AWE community.

Acknowledgements

First of all we thank Daidalos Capital for financing the hardware of our test platform. We thank Thomas Petri who as an experienced model pilot helped us to perform the first flight tests of our aircraft without tether, Tobias Schiffer for assistance during several test flights, and Roland Schmehl, Steffen Schaepe, Peter Wagner and Klaus Desch for very helpful discussions. We thank Antonello Cherubini for detailed comments on the manuscript. C. S. thanks the Experimental Particle Physics group at Bonn University, where part of this work was done, for their warm hospitality. Our biggest thanks goes to the community of open-source software development. Without the developers' spirit to share their knowledge and without the tremendous work they encoded in the free software used and adapted here, this project would not have been possible.

References

- [1] M. L. Loyd, "Crosswind kite power (for large-scale wind power production)," *Journal of Energy* 4 no. 3, (2015/09/26, 1980) 106–111. <http://dx.doi.org/10.2514/3.48021>.
- [2] U. Ahrens, M. Diehl, and R. Schmehl, eds., *Airborne Wind Energy*. Springer Science & Business Media, Berlin Heidelberg, 2013.
- [3] A. Cherubini, A. Papini, R. Vertechy, and M. Fontana, "Airborne wind energy systems: A review of the technologies," *Renewable and Sustainable Energy Reviews* 51 (2015) 1461 – 1476. <http://www.sciencedirect.com/science/article/pii/S1364032115007005>.
- [4] M. Ebrahimi Salari, J. Coleman, and D. Toal, *Airborne Wind Energy—A Review*, pp. 81–92. Springer International Publishing, Cham, 2017. http://dx.doi.org/10.1007/978-3-319-45677-5_10.
- [5] U. Zillmann, "Producing energy with ... drones?!", 2016. https://medium.com/@udo_zillmann/producing-energy-with-drones-f73a6bd0b737.

- [6] L. Fagiano, E. Van Nguyen, F. Rager, S. S., and O. C., “A small-scale prototype to study the take-off of tethered rigid aircrafts for airborne wind energy,” *CoRR abs/1608.01846* (2016) . <http://arxiv.org/abs/1608.01846>.
- [7] A. Bormann, M. Ranneberg, P. Kövesdi, C. Gebhardt, and S. Skutnik, *Development of a Three-Line Ground-Actuated Airborne Wind Energy Converter*, pp. 427–436. Springer Berlin Heidelberg, Berlin, Heidelberg, 2013. http://dx.doi.org/10.1007/978-3-642-39965-7_24.
- [8] Luchsinger, “Closing the gap: Pumping cycle kite power with twings,” 06, 2015. <http://www.awec2015.com/>. Talk at AWEC.
- [9] U. Fechner and R. Schmehl, “Design of a distributed kite power control system”. 2012 iee multi-conference on systems and control,” October, 2012. IEEE Multi-Conference on Systems and Control.
- [10] R. Ruiterkamp and S. Sieberling, *Description and Preliminary Test Results of a Six Degrees of Freedom Rigid Wing Pumping System*, pp. 443–458. Springer Berlin Heidelberg, Berlin, Heidelberg, 2013. http://dx.doi.org/10.1007/978-3-642-39965-7_26.
- [11] B. Houska and M. Diehl, “Optimal control for power generating kites,” in *In Proceedings of the 9th European Control Conference, Kos, Greece*, p. 3560–3567. 2007.
- [12] J. Stuyts, G. Horn, W. Vandermeulen, J. Driesen, and M. Diehl, “Effect of the electrical energy conversion on optimal cycles for pumping airborne wind energy,” *IEEE Transactions on Sustainable Energy* (2015) .
- [13] M. Zanon, S. Gros, and M. Diehl, “Model Predictive Control of Rigid-Airfoil Airborne Wind Energy Systems,” in *Airborne Wind Energy*, U. Ahrens, M. Diehl, and R. Schmehl, eds., pp. 219–233. Springer, 2014.
- [14] T. A. Wood, E. Ahbe, H. Hesse, and R. S. Smith, “Predictive Guidance Control for Autonomous Kites with Input Delay,” in *IFAC World Congress*. Toulouse, France, July, 2017. <http://control.ee.ethz.ch/index.cgi?page=publications;action=details;id=5622>.
- [15] E. J. Terink, J. Breukels, R. Schmehl, and W. J. Ockels, “Flight dynamics and stability of a tethered inflatable kiteplane,” *Journal of Aircraft* **48** no. 2, (2017/04/06, 2011) 503–513. <http://dx.doi.org/10.2514/1.C031108>.
- [16] M. Erhard and H. Strauch, “Control of Towing Kites for Seagoing Vessels,” *ArXiv e-prints* (Feb., 2012) , arXiv:1202.3641.
- [17] M. Erhard, G. Horn, and M. Diehl, “A quaternion-based model for optimal control of the SkySails airborne wind energy system,” *Zeitschrift für Angewandte Mathematik und Mechanik* **97** no. 1, (2017) 7–24.
- [18] T. Jörger, J. Schlagenhauf, E. Rosch, E. M., M. Dold, J. Greulich, B. Schleusener, J. Reimer, and M. Diehl, “TOPCORE open modular platform for real-time control of experimental airborne wind energy setups,” in *accepted to 20th IFAC World Congress, Toulouse, France (no preprint available)*. 2016.
- [19] S. Costello, G. François, and D. Bonvin, “Crosswind kite control - a benchmark problem for advanced control and dynamic optimization,” *European Journal of Control* (2017) –. <http://www.sciencedirect.com/science/article/pii/S0947358016300735>.
- [20] L. Fagiano, A. U. Zraggen, M. Morari, and M. Khammash, “Automatic crosswind flight of tethered wings for airborne wind energy: modeling, control design and experimental results,” *CoRR abs/1301.1064* (2013) . <http://arxiv.org/abs/1301.1064>.
- [21] E. N. Van, L. Fagiano, and S. Schnez, “Autonomous take-off and landing of a tethered aircraft: a simulation study.” <http://arxiv.org/abs/1510.01088>. arXiv:1510.01088.

-
- [22] U. Fechner and R. Schmehl, “Flight path control of kite power systems in a turbulent wind environment,” in *2016 American Control Conference (ACC)*, pp. 4083–4088. July, 2016.
- [23] U. Fechner and R. Schmehl, “Feed-forward control of kite power systems,” *Journal of Physics: Conference Series* **524** no. 1, (2014) 012081.
<http://stacks.iop.org/1742-6596/524/i=1/a=012081>.
- [24] T. Gehrman, “A development of an open-source wind drone.” 2016.
- [25] L. Meier, D. Honegger, and M. Pollefeys, “PX4: A node-based multithreaded open source robotics framework for deeply embedded platforms,” in *Robotics and Automation (ICRA), 2015 IEEE International Conference on*. May, 2015.
- [26] A. Tridgell, T. Pittenger, *et al.* <http://ardupilot.org/ardupilot/docs/common-team.html>.
- [27] Philips. <http://www.i2c-bus.org/>.
- [28] L. Meier *et al.* <http://qgroundcontrol.org/mavlink/start>.
- [29] J. S. Berndt *et al.* <http://jsbsim.sourceforge.net/>.
- [30] M. Osborne *et al.* <http://ardupilot.org/planner/docs/mission-planner-overview.html>.
- [31] B. Bonney *et al.* <http://ardupilot.org/planner2/>.
- [32] A. Tridgell *et al.* <http://ardupilot.github.io/MAVProxy/html/index.html>.
- [33] S. Park, J. Deyst, and J. P. How, “A new nonlinear guidance logic for trajectory tracking,” in *AIAA guidance, navigation, and control conference and exhibit*. 2004.
- [34] P. Riseborough *et al.* <http://ardupilot.org/dev/docs/ekf2-estimation-system.html>.